

Small droplets on superhydrophobic substrates

Markus Gross,^{1,2} Fathollah Varnik,^{1,2,*} Dierk Raabe,² and Ingo Steinbach¹

¹*Interdisciplinary Centre for Advanced Materials Simulation (ICAMS), Ruhr-Universität Bochum, Stiepelers Strasse 129, 44801 Bochum, Germany*

²*Max-Planck Institut für Eisenforschung, Max-Planck Str. 1, 40237 Düsseldorf, Germany*

(Received 28 January 2010; published 21 May 2010)

We investigate the wetting behavior of liquid droplets on rough hydrophobic substrates for the case of droplets that are of comparable size to the surface asperities. Using a simple three-dimensional analytical free-energy model, we have shown in a recent letter [M. Gross, F. Varnik, and D. Raabe, *EPL* **88**, 26002 (2009)] that, in addition to the well-known Cassie-Baxter and Wenzel states, there exists a further metastable wetting state where the droplet is immersed into the texture to a finite depth, yet not touching the bottom of the substrate. Due to this new state, a quasistatically evaporating droplet can be saved from going over to the Wenzel state and instead remains close to the top of the surface. In the present paper, we give an in-depth account of the droplet behavior based on the results of extensive computer simulations and an improved theoretical model. In particular, we show that releasing the assumption that the droplet is pinned at the outer edges of the pillars improves the analytical results for larger droplets. Interestingly, all qualitative aspects, such as the existence of an intermediate minimum and the “reentrant transition,” remain unchanged. We also give a detailed description of the evaporation process for droplets of varying sizes. Our results point out the role of droplet size for superhydrophobicity and give hints for achieving the desired wetting properties of technically produced materials.

DOI: [10.1103/PhysRevE.81.051606](https://doi.org/10.1103/PhysRevE.81.051606)

PACS number(s): 68.08.Bc, 47.55.D—

I. INTRODUCTION

As is well known, the hydrophobicity of a surface can be amplified by the existence of roughness at the micrometer level [1–3]. The phenomenon of superhydrophobicity has regained considerable interest during the last years, both due to novel industrial applications, such as self-cleaning materials, and the need for better understanding of surface-driven flows (see [4,5] for recent reviews).

On a topologically patterned surface, a liquid droplet can usually attain two possible equilibrium [6] states: it can appear either in the Cassie-Baxter (CB) state, where it is resting on top of the pillars [7], or in the Wenzel state, where the droplet penetrates into the grooves and wets the bottom substrate between the pillars [8]. In the case of droplets much larger than the typical size of the surface asperities, the free energies can be calculated by taking into account average surface properties. The relevant quantities are the surface roughness r (ratio between actual substrate area and its horizontal projection) and the surface density ϕ (portion of a planar surface of unit area covered by the asperities or pillars). On a perfectly flat and chemically homogeneous surface, the macroscopic contact angle θ is equal to the microscopic contact angle θ_Y , which—as a consequence of free-energy minimization—is dictated by Young’s law,

$$\cos \theta_Y = \frac{\sigma_{SV} - \sigma_{SL}}{\sigma_{LV}}. \quad (1)$$

Here σ_{LV} , σ_{SL} , and σ_{SV} are the surface tensions of liquid-vapor, solid-liquid, and solid-vapor interfaces, respectively. On a textured surface, on the other hand, one obtains the

macroscopic contact angle as the weighted sum

$$\cos \theta_F = \phi \cos \theta_Y - (1 - \phi), \quad (2)$$

in the case of the CB state [7], and

$$\cos \theta_W = r \cos \theta_Y,$$

in the case of the Wenzel state [8]. It can be shown [9] that the free energy of a droplet is smaller in the Cassie-Baxter as compared to the Wenzel state if

$$r > \cos \theta_F / \cos \theta_Y. \quad (3)$$

This analysis does not take into account possible free-energy barriers between the two states. However, the mere fact that more than one wetting state can occur on the same substrate implies the existence of a free-energy barrier between them [9–19]. This barrier can be overcome, for example, by applying an external force [12], giving the drop a certain impact velocity [20–22], or by increasing the pressure inside the drop [14,23,24]. Moreover, it has been found that the barrier also depends on the size of the droplet [14,24,25].

The collapse mechanism is studied in the literature mostly by depositing the droplet initially in the CB state and letting it slowly evaporate. When the droplet shrinks, the curvature of the liquid-vapor interface increases; hence, the lower part of the droplet approaches the bottom surface. On small pillars, this can lead to the nucleation of contact between the liquid and the substrate while the sidewalls of pillars are completely dry, i.e., the droplet is still in the CB state. However, as soon as a contact is nucleated, the liquid spreads and fills the entire groove, thereby taking on the Wenzel state. On taller pillars, the Laplace pressure will eventually lead to a depinning of the lower contact line and the droplet slides down the pillars [26,27].

*fathollah.varnik@rub.de

It is clear that a droplet which is of the same size as the surface structures will directly feel the geometry of the substrate, and therefore considering merely averaged surface properties might be not sufficient anymore [28–31]. Due to the fact that these droplets have typical radii on the order of microns they are subject to fast evaporation and have a very short lifetime. This makes them very hard to observe in direct experiment and, not surprisingly, the literature has so far provided only a few hints on their behavior [19,26,30,32,33].

Notably, Ref. [30] concentrated on the particular case of droplets of comparable size to the surface structures. However, the droplets considered, having typical radii of $\sim 1000\ \mu\text{m}$, were still comparatively large to the pillar distance ($\sim 200\ \mu\text{m}$) and height ($\sim 100\ \mu\text{m}$). It was observed that on moderately rough (i.e., small r) structures the Wenzel state is energetically favored, while for increased roughness droplets typically adopted a CB state (geometry-induced transition). In a recent molecular-dynamics study of nano-scale droplets on a pillared surface [19] the influence of several geometric parameters on the wetting behavior was investigated. It was found that, if the pillar height exceeds a critical size, both Wenzel and Cassie-Baxter states can coexist due to a pronounced free-energy barrier. For smaller pillars, however, the droplet typically preferred only one of the two states, in agreement with previous investigations [26,30].

It has only recently been shown by us [34] that a small droplet can, besides in the Wenzel and CB states, also occur in a third previously unrecognized equilibrium state. This state is characterized by a finite immersion depth of the droplet into the texture, yet without contact to the bottom substrate. The existence of this state can be inferred from quite general arguments and hence is expected to be largely independent of the particular surface geometry, provided only that the asperities are large enough to prevent contact of the droplet with the bottom substrate.

We emphasize again that it is important to realize that this state, which we choose to call *impaled state*, is different from the previously known “partially impaled” conformations of the CB state, where the liquid-vapor interface below the macroscopic contact line is curved, but the droplet essentially remains on top of the asperities [23,24]. This statement is supported by the fact that we indeed find a coexistence regime for the new impaled state and the (partially impaled) CB state. We have demonstrated that by virtue of this new state, a droplet can pass through a reentrant transition upon, e.g., evaporation, having in fact been saved from adopting a Wenzel state [34].

Droplets of similar size to the roughness scale occur in any evaporation or condensation process and therefore are important for the understanding of many natural phenomena such as, for example, the water repellency of many plant leaves or insect eyes. On the other hand, the efficiency of a self-cleaning surface decisively depends on its condensation resistance and its ability to keep both large and small droplets close to the top of the roughness structures, i.e., in a CB state. The situation we consider in this paper may also be relevant for numerous industrial processes such as ink jet printing and spray coating, where droplets can be as small as the roughness patterns of the substrate.

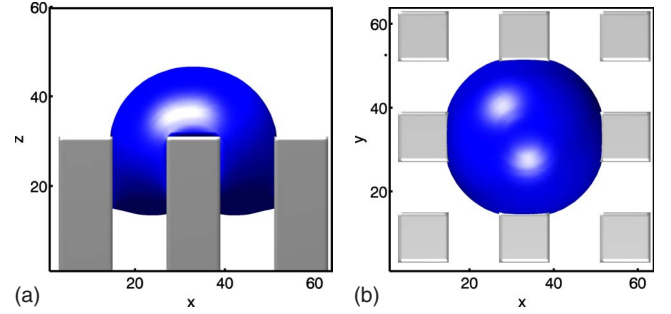


FIG. 1. (Color online) A typical small droplet suspended on a hydrophobic pillar array, as viewed (a) from the side and (b) from the top. The above plots are taken from one of our lattice Boltzmann simulations.

In the present work, we extend our previous study [34] and investigate the specific behavior of small droplets on a regularly pillared hydrophobic surface. For this purpose, we have performed extensive numerical computer simulations using the lattice Boltzmann (LB) method in three dimensions [35–37]. The analytical three-dimensional free-energy model introduced previously [34] is thoroughly discussed and suitably extended to account for the observed deviations. Furthermore, we will study the properties of the free-energy barrier for a droplet in the CB state and investigate its dependence on the contact angle and droplet size.

The size scale of the droplet and the roughness features are in the range between $0.1\ \mu\text{m}$ and $1\ \text{mm}$ (see Sec. II A 2), so that thermal fluctuations and gravity can be safely neglected and a simple macroscopic description is possible. Figure 1 is taken from one of our simulations and shows a typical situation that we consider in this work.

Note that while the considered droplet configuration (Fig. 1) looks apparently special, further simulations by us have shown that it is in fact stable against moderate perturbations [38]. In particular, the central pillar is just included for practical reasons, namely, in order to conveniently observe a CB state even for very small droplets. Despite that, it will become clear that all the essential predictions of our work can be expected to hold for any similar configuration and geometry.

In addition to the fully static situation, we also discuss the case of quasistatically evaporating droplets. Here, we elaborate on our previous proposition of a reentrant transition, in which—due to the specific properties of the new impaled state—the evaporating droplet never sinks down the pillars completely. Instead, it remains close to the top of the texture and, if it is small enough, even dissolves from the pillar sidewalls. This observation is of great practical relevance for the fabrication of efficient self-cleaning surfaces where droplets in the Wenzel state have a detrimental effect [39].

II. THEORY

A. Numerical model

In order to study a two-phase liquid-vapor system, we employ a free-energy-based lattice Boltzmann method first introduced in [40] and later extended [35,36] to include wet-

ting on substrates. We will first review the thermodynamics involved in the method and then briefly describe how it is implemented in a lattice Boltzmann scheme.

1. Thermodynamics

The thermodynamic equilibrium of a two-phase liquid-vapor system including a substrate is determined by a Cahn-Hilliard-type free-energy functional of the form

$$\Psi = \int_{\text{vol}} \left(\psi_b(\rho) + \frac{\kappa}{2} (\partial_\alpha \rho)^2 \right) dV + \int_{\text{surf}} \psi_s(\rho_s) dS.$$

Here, ψ_b is the bulk free energy of each of the two phases, ψ_s is the surface free energy, and ρ_s is the density at the surface (see, e.g., [41]). The second term in the first integral gives the free-energy contribution due to density gradients in an inhomogeneous system and κ is a parameter that tunes the surface tension and interface width. The second integral just runs over the substrate surface and accounts for the short-ranged fluid-solid interactions, according to the mean-field framework of Cahn [42].

To solve the free-energy model we have to specify the two free-energy densities ψ_b and ψ_s . We take the bulk free energy to be of a simple double-well form [35],

$$\psi_b(\rho) = p_c(\nu_\rho + 1)^2(\nu_\rho^2 - 2\nu_\rho + 3 - 2\beta\nu_T), \quad (4)$$

yielding the equation of state for the fluid,

$$p_b = p_c(\nu_\rho + 1)^2(3\nu_\rho^2 - 2\nu_\rho + 1 - 2\beta\nu_T).$$

Here, $\nu_\rho = (\rho - \rho_c)/\rho_c$ is the reduced density; $\nu_T = (T_c - T)/T_c$ is the reduced temperature; and $\rho_c = 7/2$, $p_c = 1/8$, and $T_c = 4/7$ are the critical density, pressure, and temperature, respectively. The parameter β is a constant that is related to the density difference between the two phases and will be set to 0.1 in this work. Below T_c , the model allows liquid and vapor to coexist in equilibrium with densities

$$\rho_{l,v} = \rho_c(1 \pm \sqrt{\beta\nu_T}).$$

The liquid-vapor surface tension and interface width in this model are calculated to be

$$\sigma_{LV} = \frac{4}{3} \sqrt{2\kappa p_c} (\beta\nu_T)^{3/2} \rho_c,$$

$$\xi = \sqrt{\kappa \rho_c^2 / 4\beta\nu_T p_c}.$$

Following [42], the surface free energy ψ_s is commonly approximated as $\psi_s(\rho_s) = -\phi_1 \rho_s$. The constant ϕ_1 , called wetting potential, determines the interaction between fluid and substrate. Minimization of the free-energy functional leads to a boundary condition for the density gradient in the direction perpendicular to the substrate,

$$\kappa \partial_\perp \rho = -\phi_1. \quad (5)$$

The wetting potential itself can be related to the equilibrium Young contact angle θ_Y via

$$\phi_1 = 2\beta\nu_T \sqrt{2p_c \kappa} \operatorname{sgn}\left(\frac{\pi}{2} - \theta_Y\right) \sqrt{\cos\frac{\alpha}{3} \left(1 - \cos\frac{\alpha}{3}\right)},$$

with $\alpha = \arccos(\sin^2 \theta_Y)$. As shown in [42], the liquid-solid and solid-vapor surface tensions can be calculated from the liquid-vapor surface tension and the wetting potential, i.e., κ and θ_Y alone.

2. Lattice Boltzmann method

The lattice Boltzmann algorithm solves the Navier-Stokes equations via a space and time discretized version of the Boltzmann kinetic equation (for an introduction, see, e.g., [43,44]). The continuity and Navier-Stokes equations for an inhomogeneous fluid read

$$\partial_t \rho + \partial_\alpha (\rho u_\alpha) = 0,$$

$$\partial_t (\rho u_\alpha) + \partial_\beta (\rho u_\alpha u_\beta) = -\partial_\beta P_{\alpha\beta} + \nu \partial_\beta [\rho (\partial_\beta u_\alpha + \partial_\alpha u_\beta + \delta_{\alpha\beta} \partial_\gamma u_\gamma)],$$

where ρ is the density and u_a is the local fluid velocity. The thermodynamic equilibrium constraints of our model are included in the hydrodynamic equations through the boundary condition (5) and the pressure tensor $P_{\alpha\beta}$. The choice (4) for the free energy leads to

$$P_{\alpha\beta} = \left(p_b - \frac{\kappa}{2} (\partial_\alpha \rho)^2 - \kappa \rho \partial_\gamma \rho \right) \delta_{\alpha\beta} + \kappa (\partial_\alpha \rho) (\partial_\beta \rho).$$

In our work, we employ a D3Q15 lattice Boltzmann model, that is, we use three-dimensional spatial grid with 15 discrete velocity vectors \mathbf{c}_i on each lattice site. The dynamical quantity here is the one-particle distribution function $f_i(\mathbf{r}, t)$ ($i=0, \dots, 15$) which evolves according to the lattice Boltzmann equation

$$f_i(\mathbf{r} + \mathbf{c}_i \Delta t, t + \Delta t) = f_i(\mathbf{r}, t) + \frac{\Delta t}{\tau} [f_i^{\text{eq}}(\mathbf{r}, t) - f_i(\mathbf{r}, t)].$$

Here, Δt ($\equiv 1$) is the time step of the simulation and τ is the relaxation time. We have neglected any terms due to a body-force-like gravitation as we will not consider these influences in the present work. The relaxation time is related to the kinematic viscosity ν_{LB} (in lattice Boltzmann units) through

$$\nu_{LB} = \frac{1}{3} \left(\tau - \frac{1}{2} \right).$$

The thermodynamic conditions are implemented via the pressure tensor by constraining the moments of the equilibrium distribution function f_i^{eq} ,

$$\sum_i f_i^{\text{eq}} = \rho, \quad \sum_i f_i^{\text{eq}} c_{i\alpha} = \rho u_{i\alpha},$$

$$\sum_i f_i^{\text{eq}} c_{i\alpha} c_{i\beta} = P_{\alpha\beta} + \rho u_\alpha u_\beta + \nu [u_\alpha \partial_\beta \rho + u_\beta \partial_\alpha \rho + u_\gamma (\partial_\gamma \rho) \delta_{\alpha\beta}].$$

For further details on the implementation and on the wetting boundary conditions the reader is referred to [35,36].

Units. Since in our simulations we are dealing exclusively

with dimensionless lattice units, it is necessary to give the conversion factors to physical units (see also [36]). The value of quantity with dimensions $L^a T^b M^c$ obtained from the LB simulation has to be multiplied by a suitable combination of conversion factors, $(\Delta l)^a (\Delta t)^b (\Delta m)^c$, in order to find its value in physical units. The conversion factors Δl , Δt , and Δm are determined using the experimentally known values of the density $\rho_{\text{phys}} [\text{kg/m}^3]$, viscosity $\nu_{\text{phys}} [\text{m}^2/\text{s}]$, and surface tension $\sigma_{\text{phys}} = \sigma_{\text{LV}} [\text{kg/s}^2]$ of the liquid under consideration. These quantities are related to the corresponding known lattice Boltzmann variables ρ_{LB} , ν_{LB} , and σ_{LB} via

$$\rho_{\text{phys}} = \frac{\Delta m}{\Delta l^3} \rho_{\text{LB}}, \quad \nu_{\text{phys}} = \frac{\Delta l^2}{\Delta t} \nu_{\text{LB}}, \quad \sigma_{\text{phys}} = \frac{\Delta m}{\Delta t^2} \sigma_{\text{LB}}.$$

Solving this system of equations for Δl , Δt , and Δm one finds

$$\begin{aligned} \Delta l &= \frac{\rho_{\text{phys}}}{\rho_{\text{LB}}} \left(\frac{\nu_{\text{phys}}}{\nu_{\text{LB}}} \right)^2 \frac{\sigma_{\text{LB}}}{\sigma_{\text{phys}}}, \\ \Delta t &= \left(\frac{\rho_{\text{phys}}}{\rho_{\text{LB}}} \right)^2 \left(\frac{\nu_{\text{phys}}}{\nu_{\text{LB}}} \right)^3 \left(\frac{\sigma_{\text{LB}}}{\sigma_{\text{phys}}} \right)^2, \\ \Delta m &= \left(\frac{\rho_{\text{phys}}}{\rho_{\text{LB}}} \right)^4 \left(\frac{\nu_{\text{phys}}}{\nu_{\text{LB}}} \right)^6 \left(\frac{\sigma_{\text{LB}}}{\sigma_{\text{phys}}} \right)^3. \end{aligned}$$

In all the simulations reported in this paper, the values of the lattice Boltzmann parameters are fixed to be

$$\rho_{\text{LB}} = 4.1, \quad \nu_{\text{LB}} = 0.1, \quad \sigma_{\text{LB}} = 5.4 \times 10^{-4}, \quad (6)$$

where the value of σ_{LB} results from a choice of $\kappa=0.002$. If we now take, for example, silicone oil as the physical counterpart,

$$\begin{aligned} \rho_{\text{phys}} &= 10^3 \text{ kg/m}^3, \quad \nu_{\text{phys}} = 5 \times 10^{-5} \text{ m}^2/\text{s}, \\ \sigma_{\text{phys}} &= 0.02 \text{ kg/s}^2, \end{aligned} \quad (7)$$

we obtain

$$\begin{aligned} \Delta l &= 1.6 \times 10^{-6} \text{ m/lattice distance}, \\ \Delta t &= 5.4 \times 10^{-9} \text{ s/lattice time}, \\ \Delta m &= 1.1 \times 10^{-15} \text{ kg/mass unit}. \end{aligned} \quad (8)$$

For convenience, we also state the conversion factor for energy,

$$\Delta E = \frac{\Delta l^2 \Delta m}{\Delta t^2} = 7.0 \times 10^{-11} \text{ J/lattice unit}.$$

Thus, for the above choice of physical parameters our simulated droplets would be of micron scale. Note that it is not directly possible to assume, for example, water as the simulated liquid since the low viscosity and large surface tension would lead to Δl of order 10^{-10} m/lattice distance. That in turn would mean that we would have to increase the number of lattice sites by a factor of 10^6 in order to simulate micron-sized water droplets, an option that is not computa-

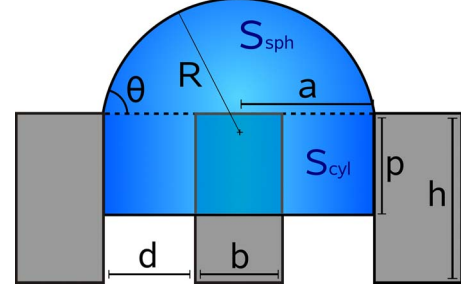


FIG. 2. (Color online) Cross section through a droplet suspended on a pillar array as described by our analytical model. The droplet is assumed to be pinned at the edges of the pillars, i.e., has a fixed base radius a . For a given droplet size, the only way to minimize the overall free energy is thus via a change in the penetration depth p . This also fixes the apparent contact angle θ .

tionally feasible. However, since in our case the only effect of viscosity is to change the relaxation time of the fluid, we expect the results in this work to be valid for all kinds of Newtonian liquids.

An important natural scale in the physics of liquid interfaces is the capillary velocity $u_c = \sigma/(\nu\rho)$ and the associated capillary time $t_c = l/u_c$, where l is a typical length scale in the system. t_c can be understood as the characteristic time over which a disturbance in the liquid-vapor interface is expected to be smoothed out. Taking $l \approx 10$ lattice units, which is the order of the size of a droplet in our simulations, we obtain for the above set of parameters (6) and (7) a value of $t_{c,\text{LB}} = 7.6 \times 10^3$, corresponding to $t_{c,\text{phys}} = 4.1 \times 10^{-5}$ s. For convenience, we will normalize all our simulation times to $10^4 \approx t_{c,\text{LB}}$ time steps.

B. Analytical model

1. Introduction

Geometry. We use a simple macroscopic three-dimensional model for a droplet suspended on an array of cuboidal posts with width b , height h , and distance d between each other. Gravity will be neglected in this work since we are considering droplets that are smaller than the capillary length $k^{-1} = \sqrt{\sigma/g\rho}$, which is about 1.4 mm for our choice of parameters (7). Looking at an equilibrium configuration of a typical droplet in our simulation (Fig. 1), we see that we can well approximate the part of the droplet which is located above the posts as a spherical cap with base

$$a = \frac{1}{2}(b + 2d) = R \sin \theta,$$

where R is the radius of the cap (Fig. 2). The impaled part is modeled as a cylinder with radius a and height p (penetration depth), surrounding the central pillar. In this model, the Wenzel state would correspond to $p=h$ and the CB state to $p=0$.

In the simplest version of this model, we assume the macroscopic contact line of the droplet to be pinned at the edges of the outer pillars. In a subsequent refinement, we shall relax this condition and allow the base radius a to vary. Following the simple argument of Gibbs [45], θ can vary be-

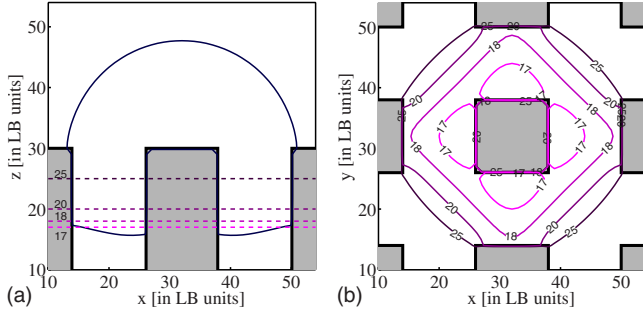


FIG. 3. (Color online) Geometry of the droplet as observed in our simulations. (a) shows a cross section of the droplet and (b) shows the liquid-vapor interface at different z values [marked in (a)]. It is clearly seen that especially close to the bottom of the droplet the approximation of its shape by a cylinder becomes increasingly imprecise.

tween the value of the advancing contact angle $\theta_a = \theta_{a,\text{flat}} = \theta_Y$ and the receding contact angle $\theta_r = \theta_{r,\text{flat}} - 90^\circ = \theta_Y - 90^\circ$. In general, the macroscopic contact angle θ is different from the equilibrium Young contact angle θ_Y of a droplet on a flat surface. Note that in this work we only consider hydrophobic substrates ($\theta_Y > 90^\circ$).

The simplifications of our model in particular entail the neglect of the curvature in the bottom region of the droplet. In reality, this part is not a cylinder but instead adopts the shape of a minimal surface spanned by the pillars, rendering its geometry highly nontrivial and hard to capture exactly in an analytical form (see Fig. 3). As a consequence, the overall liquid surface in our analytical model is slightly larger than it would be in reality and in our simulations. Also, the cylinder part of our model droplet contributes slightly too much to the total volume compared to the spherical cap part.

The volume of the droplet (cap and cylinder) shall be fixed,

$$V_0 = \text{const} = V_{\text{sph}}(\theta) + V_{\text{cyl}}(p), \quad (9)$$

with

$$V_{\text{sph}} = \frac{1}{3} \pi a^3 \frac{2 - 3 \cos \theta + \cos^3 \theta}{\sin^3 \theta}, \quad V_{\text{cyl}} = (\pi a^2 - b^2)p,$$

being the volume of the cap and the penetrating cylinder, respectively. Note that when we speak of the *size* of a droplet, we usually mean the *effective radius* R_{eff} that corresponds to a given volume V_0 . The quantity R_{eff} is thus to be distinguished from the radius of the spherical cap R .

Since we are interested in the dependence of the droplet free energy on the penetration depth p , we consider p as our free variable and determine the dependence of θ on p via the fixed volume condition (9). As the corresponding analytical expression $\theta(p)$ is rather lengthy, we will not state it here. The surface area of the spherical cap and the lateral surface area of the cylinder that is not covered by the pillars are given by

$$S_{\text{sph}} = 2\pi a^2 \frac{1 - \cos \theta(p)}{\sin^2 \theta(p)}, \quad S_{\text{cyl}} = (2\pi a - 4b)p,$$

respectively. Note that the above expressions for V_{sph} and S_{sph} are valid for arbitrary angles of θ between 0° and 180° .

Free energy. Since the volume of the drop is constant, only surface free-energy contributions play a role in the present problem. The free energy of a suspended droplet in our model, neglecting gravity, is given by

$$F(p) = \sigma_{\text{LV}}(S_{\text{sph}}(\theta, a) + S_{\text{cyl}}(p, a) + \underbrace{S_{\text{bot}}(a)}_{\text{for } p < h}) + \sigma_{\text{SL}}(8bp + \underbrace{S_{\text{bot}}(a)}_{\text{for } p = h}) + \sigma_{\text{SV}}(8b(h - p) + \underbrace{S_{\text{bot}}(a)}_{\text{for } p < h}), \quad (10)$$

where $S_{\text{bot}} = \pi a^2 - b^2$ is the area of the liquid-vapor interface on the bottom of the droplet cylinder. The horizontal braces indicate that the corresponding terms should only be included when $p < h$ or $p = h$, respectively. Since the relevant quantity is the reduced free energy $f(p) \equiv F(p) - F(0)$, we have already neglected all trivial constant contributions to F . With the help of the Young relation (1), the reduced free energy can be finally written as

$$f(p) = \sigma_{\text{LV}}(S_{\text{sph}}(\theta) - S_{\text{sph}}|_{p=0} + S_{\text{cyl}}(p) - 8bp \cos \theta_Y - \underbrace{S_{\text{bot}}}_{\text{for } p=h} (1 + \cos \theta_Y)). \quad (11)$$

As expected, the free energy can be evaluated knowing σ_{LV} and θ_Y alone. Moreover, the free energy is scale invariant: if all length scales are increased by a factor of x , f just changes by a factor of x^2 due to the presence of the surface terms. This is a consequence of the fact that no volume term appears in f . Thus, changing the system size is equivalent to changing the measurement units with no effect on the physics. Hence, our model is applicable to droplet phenomena on any length scale as long as the droplet is small enough to neglect the influence of gravity (and large enough to neglect thermal fluctuations).

The term proportional to S_{bot} represents the free-energy change when the droplet reaches the bottom substrate and the liquid-vapor and solid-vapor interfaces are replaced with one single solid-liquid interface. In reality, due to the curvature of the lower interface, this transition would not happen immediately but instead there will be some small part of the liquid first contacting the substrate and this contact line will then propagate outward [46]. The final reduction in free energy due to the Wenzel transition is given by

$$\Delta E_{\text{Wenzel}} = S_{\text{bot}}[\sigma_{\text{SL}} - (\sigma_{\text{LV}} + \sigma_{\text{SV}})] = -S_{\text{bot}}\sigma_{\text{LV}}(1 + \cos \theta_Y), \quad (12)$$

which is always negative and hence the Wenzel state is at least metastable.

2. Predictions

Free-energy landscape. In Fig. 4 we plot the dependence of the free energy on the penetration depth p for varying Young contact angles and droplet radii. We observe several

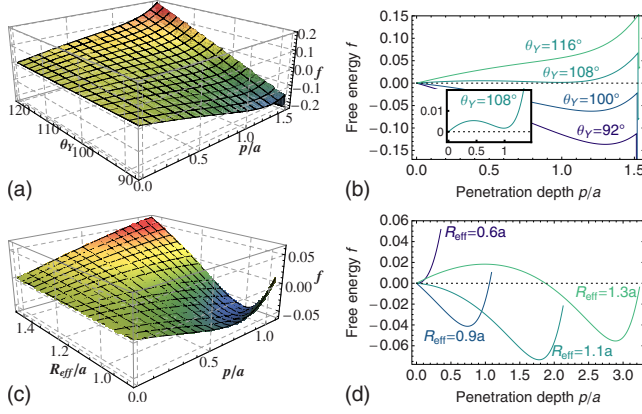


FIG. 4. (Color online) Free-energy landscape for a droplet in our analytical model (left panels) together with cuts along the p direction for sample values of the parameters (right panels), for a surface geometry of $b/d=1$. Except for the lower left plot, all curves are drawn up to the point ($p \approx 1.5a$) where no further liquid remains in the spherical cap. (a) and (b) Dependence of the free energy $f/4\pi a^2 \sigma_{LV}$ on the penetration depth p and the Young contact angle θ_Y for a droplet of fixed size $R_{\text{eff}}=a$. The vertical streaks at the right end of the curves indicate the free-energy loss $-\Delta E_{\text{Wenzel}}$ [Eq. (12)] in case a transition to the Wenzel state would occur at $p \approx 1.5a$. (c) and (d) Dependence of the free energy $f/4\pi a^2 \sigma_{LV}$ on the penetration depth p and the droplet size R_{eff} for a contact angle of $\theta_Y = 100^\circ$. Note the appearance of a free-energy barrier between the CB and partially impaled state with increasing droplet size.

interesting features: first, the intrinsic stability of the CB state, determined by the slope of f at $p=0$, depends on both the contact angle and the size of the droplet. This fact is well known from previous studies [14,23–26,47]. However, it must be added that in experiments it is typically hard to differentiate between the Wenzel transitions due to the intrinsic instability as compared to nucleation of contact.

Second, and more remarkably, the free energy can have a *local minimum* at a finite penetration depth that exists in addition to the minima associated with the CB and Wenzel states. Given that θ_Y is smaller than a certain value (calculated below), the intermediate minimum occurs for any droplet size, but the corresponding penetration depth p_{min} decreases with decreasing R_{eff} [see Figs. 4(c) and 4(d)]. Although the existence of this metastable state has only recently been described in the literature [34], its implications for the wettability behavior of droplets are crucial, as will be detailed below.

Stability of the Cassie-Baxter state. The CB state is locally stable (i.e., metastable) in this model if $df/dp|_{p=0} > 0$, where

$$\frac{df}{dp} = \sigma_{LV} \left(\frac{dS_{\text{sph}}}{dp} + (2\pi a - 4b) - 8b \cos \theta_Y \right). \quad (13)$$

Note that from now on we will neglect the term proportional to S_{bot} , which is responsible for the Wenzel transition, in Eq. (11) since it will merely lead to a complicated nonanalytical behavior of the free energy and does not provide any further insights. In order to evaluate dS_{sph}/dp we first calculate $d\theta/dp$ with the help of the fixed volume condition (9),

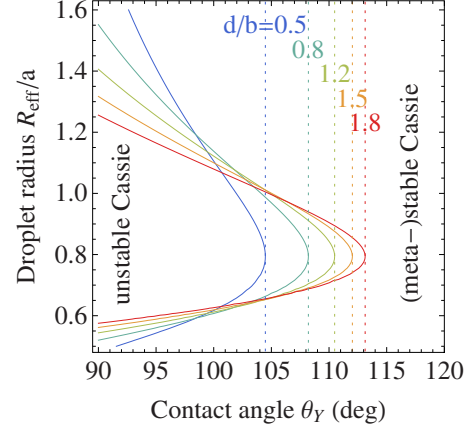


FIG. 5. (Color online) Regions of stability for the CB state. We fix the pillar width b and plot the set of points $(R_{\text{eff}}, \theta_Y)$ fulfilling $df/dp(R_{\text{eff}}, \theta_Y)|_{p=0} = 0$, for varying values of the mutual pillar distance d (solid curves). The CB state is stable to the right-hand side of each solid curve. The dotted lines mark the limiting value of θ_Y for the existence of a local minimum of the free energy [see Eq. (15)].

$$\begin{aligned} \frac{dV_0}{dp} = 0 &= \frac{dV_{\text{sph}}}{dp} + \frac{dV_{\text{cyl}}}{dp} \Rightarrow \frac{d\theta}{dp} = - \frac{dV_{\text{cyl}}}{dp} \bigg/ \frac{dV_{\text{sph}}}{d\theta} \\ &= 4 \cos^4 \frac{\theta}{2} \left(\frac{b^2}{a\pi} - a \right). \end{aligned}$$

This gives

$$\frac{dS_{\text{sph}}}{dp} = \frac{dS_{\text{sph}}}{d\theta} \frac{d\theta}{dp} = 4a \sin \frac{\theta}{2} \cos \frac{\theta}{2} \left(\frac{b^2}{a^2} - \pi \right).$$

Using the expression for $\theta(p)$ at $p=0$ enables us to determine the region in the θ_Y - R_{eff} plane where the CB state is metastable, that is, the set of points where $df/dp(R_{\text{eff}}, \theta_Y)|_{p=0} > 0$. Due to the scale invariance of the free energy, this region depends on the geometry of the pillar array only through the ratio of the mutual pillar distance b to the pillar width d .

We see (Fig. 5) that for very small droplets compared to the base length $a=b+d$, the model predicts a stable CB state even for Young contact angles close to 90° . Physically, this is understandable because the surface of the cap of such droplets is almost flat and hence does not exert any significant impalement inducing force. From our model point of view, this behavior arises from the fact that the local minimum of the free energy shifts continuously to $p=0$ [Figs. 4(c) and 4(d)]; hence, the impaled state now effectively appears as a CB state and the phase boundaries for the impaled and CB state are identical. In that situation, the CB state becomes the only possible state.

Droplets very large compared to a will also have a wide region of stability since the decrease in free energy due to a reduction in the liquid-vapor surface area of the large spherical cap cannot compensate anymore the free-energy increase resulting from the gain in liquid-solid contact area of the penetrating cylinder. As is suggested in Fig. 5 and will be

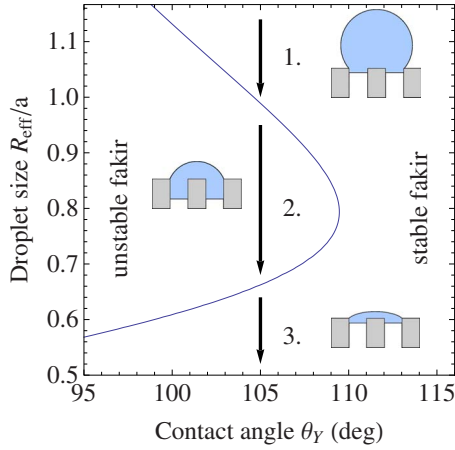


FIG. 6. (Color online) Reentrant transition. Given a moderate contact angle, a large droplet is predicted by our analytical model to assume a metastable CB state (stage 1). On reduction of its size the CB state becomes unstable and the droplet penetrates into the grooves (stage 2). If the height of the pillars prohibits a Wenzel transition, the droplet eventually enters the CB state again upon further reduction in its size (stage 3). The boundary curve of the CB stability region is shown for the case $b=d$.

proven analytically in the next section, there is never an unstable CB state in the region where no free-energy minimum exists.

As becomes clear from Fig. 5, the shape of the stability region of the CB state is largely independent of the geometry, and its characteristic shape offers the interesting possibility of a reentrant transition (Fig. 6): for a given Young contact angle, imagine a droplet that is very large and initially deposited at the top of the pillar array. According to our analytical model, the droplet will adopt a metastable CB state (stage 1 in Fig. 6). If the droplet is now reduced in size (e.g., through evaporation) and the Young contact angle is not too large, the droplet will enter the region of CB instability (stage 2). Depending on the tallness of the pillars, the droplet will now either go over into the Wenzel state or the impaled state. In the latter case, further reduction in the droplet's size brings it back again into the CB state (stage 3). This remarkable behavior is due to the peculiar dependence of the position of the intermediate minimum of the free energy on droplet size [Figs. 4(c) and 4(d)]. This aspect will become clearer in the following section.

The existence of a reentrant transition can explain some recent experimental observations, where small evaporating droplets are found to remain close to the top of the substrate [26,48] and not get trapped inside the texture. Interestingly, a recent suggestion of “immortal” CB states [23] was based on the speculative assumption that a droplet *remains* in a CB state independent of its size. However, we find that this only holds in the region of the phase diagram where no impaled state exists (regions to the right of vertical dashed lines in Fig. 5).

Intermediate minimum of the free energy. As already noted, an unstable CB state does not necessarily mean that the droplet goes over into the Wenzel state since the free energy can have a minimum before the droplet reaches the

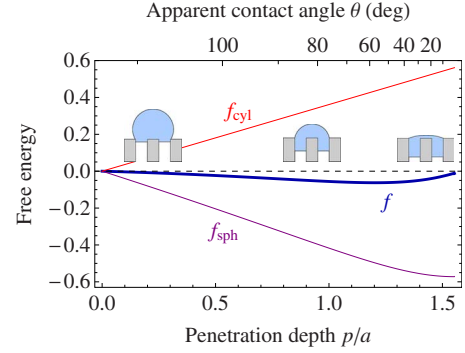


FIG. 7. (Color online) Contributions to the surface free energy $f(p)$ of the model droplet, for $R_{\text{eff}}=a$, $\theta_Y=100^\circ$, and $b/d=1$. f_{sph} and f_{cyl} are the surface free energies of the spherical cap (liquid-vapor) and cylinder part (liquid-vapor and liquid-solid), respectively. The upper abscissa gives the apparent contact angle of the spherical cap.

bottom. Local minima of the free energy can of course always be induced by local defects on the pillar sidewalls, in which case the droplet would pin at the defect. It will, however, be demonstrated that in the present case, the local minimum is of very general nature, largely independent of the particular geometry.

To understand the origin of the intermediate minimum, we split up the free energy [Eq. (11)] as $f(p)=f_{\text{sph}}(p)+f_{\text{cyl}}(p)$, where $f_{\text{sph}}(p)=\sigma_{\text{LV}}[S_{\text{sph}}(p)-S_{\text{sph}}(0)]$ represents the contribution of the spherical cap and $f_{\text{cyl}}(p)=\sigma_{\text{LV}}[S_{\text{cyl,LV}}(p)-8bp \cos \theta_Y]=\sigma_{\text{LV}}[2\pi a-4b(1+2 \cos \theta_Y)]p$ represents the contribution of the cylinder (Fig. 7). It becomes now evident that the intermediate minimum of the free energy appears due to the fact that, with increasing penetration depth, the surface of the spherical cap decreases in a nonlinear fashion, while the surface of the cylindrical part just increases linearly. In particular, when the droplet has penetrated deep enough into the grooves, almost no liquid volume remains in the spherical cap, which then becomes nearly flat. In this regime, f_{sph} decreases only slightly with increasing p and consequently f_{cyl} dominates the total free energy. Note that f_{sph} depends only on the droplet size and substrate geometry and not on the Young contact angle [49]. Therefore, the dependence of the local minimum on the contact angle is due to the change in the slope of f_{cyl} .

A more general understanding can be gained by imagining the pillars to represent a (partly open) hydrophobic capillary tube that is wetted by a droplet placed at its entry. In this situation, the equilibrium state of the droplet is a consequence of the balance between the Laplace pressure within the spherical cap (pushing the droplet into the capillary) and an opposing capillary force due to the hydrophobic substrate and the penetrating liquid. This simple reasoning in fact suggests that the intermediate minimum constitutes a generic equilibrium state of a droplet, occurring in any situation of filling a hydrophobic capillary by a spherical liquid reservoir.

In order to determine the position of the minimum, we solve $df/dp=0$ for θ which then in turn will give p by means of the fixed volume condition (9). Defining $x=\cos \theta/2$, we obtain

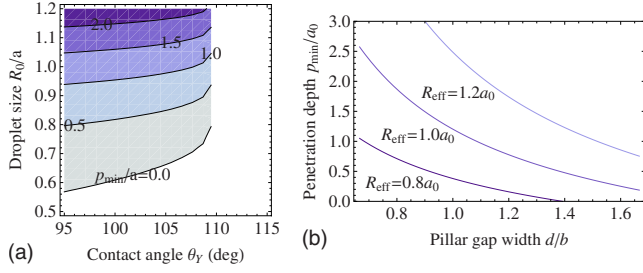


FIG. 8. (Color online) Existence region of the intermediate minimum. In (a) the penetration depth (in units of a) at which the intermediate minimum occurs is plotted for varying droplet sizes and contact angles, keeping $b=d$ (corresponding to $\theta_Y^{\text{lim}} = 109.5^\circ$). In the white region, only the CB state is stable. In (b) we plot the penetration depth [normalized to the same fixed value a that was used in part (a)] for varying ratios of the gap size d to the pillar width b .

$$\begin{aligned} \frac{df}{dp} = 0 &= 4a \left(\frac{b^2}{a^2} - \pi \right) x \sqrt{1-x^2} + (2\pi a - 4b) - 8b \cos \theta_Y \\ \Rightarrow (1-x^2)x^2 &= \left(\frac{2ab(1+2\cos\theta_Y) - a^2\pi}{2(\pi a^2 - b^2)} \right)^2. \end{aligned} \quad (14)$$

This is a quadratic equation in x^2 and the necessary condition for the existence of a solution follows from the positivity of its discriminant. We thus find that the minimum exists if

$$\theta_Y < \theta_Y^{\text{lim}} = \arccos\left(-\frac{1}{2} + \frac{b}{4a}\right). \quad (15)$$

As previous plots already have suggested, this condition does only depend on the geometry of the pillar array through the ratio of the pillar to gap width b/d . Equation (14) admits for four solutions for θ in the range $0-\pi$ of which at most two are compatible with the fixed volume condition. The solution with the smaller value of θ represents the minimum of the free energy.

In Fig. 8(a) we plot the corresponding penetration depth p_{\min} for the case $b=d$, equivalent to a value of $\theta_Y^{\text{lim}} = 109.5^\circ$. Increasing θ_Y at constant droplet size leads to a smaller penetration depth at the intermediate minimum as the tendency for the droplet to move into the CB state is increased. Correspondingly, keeping the contact angle fixed, it is seen that the penetration depth increases with the droplet size. Of course, if the pillars are shorter than p_{\min} , the droplet undergoes a Wenzel transition before ever reaching the local minimum. Since in practice the pillars cannot be made arbitrarily high, the local minimum will only be relevant for small droplets, i.e., of size $R_{\text{eff}} \lesssim h$.

For constant droplet size and pillar width, the increase in the gap size d between the pillars has two main effects: first, the penetration depth at the free-energy minimum is drastically reduced, i.e., a droplet in the intermediate minimum remains closer to the top of the pillar array [Fig. 8(b)]. Second, an increase in d leads to a reduction in the pillar density ϕ , whereby the effective contact angle in the CB state is increased [see Eq. (2)]. On the other hand, a large gap size implies a strongly bulged bottom part of a CB droplet, more

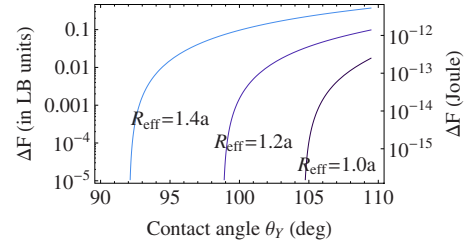


FIG. 9. (Color online) Height ΔF of the free-energy barrier between the CB state and the intermediate minimum for the case $b=d=12$ and different droplet sizes R_{eff} . On the left ordinate axis the free energy is given in LB units, while on the right side it is given in joules, using a typical set of the conversion factors.

easily inducing a Wenzel transition if the pillars are not sufficiently high. Therefore, as long as the pillars are sufficiently tall, increasing the pillar distance can be considered as favorable for the efficiency of self-cleaning surfaces.

Free-energy barrier. If a local minimum of the free energy exists, the metastability of the CB state depends on the local *maximum* of the free energy that occurs at a smaller penetration depth. Then the other valid solution of Eq. (14) corresponds to such a local maximum. Here, the necessary conditions for its existence are inequality (15) and the additional condition $df/dp|_{p=0} > 0$.

In order to induce a transition from a metastable CB state to the intermediate minimum or Wenzel state, one has to apply on the droplet an amount of work that is equal to the height of the free-energy barrier $\Delta F = F(p_{\max}) - F(0) = f(p_{\max})$. This quantity is displayed for several droplet sizes in Fig. 9, both in lattice Boltzmann and physical units (joules). The conversion factors used are given in Eq. (8).

III. SIMULATION RESULTS

We now compare the predictions of our analytical model with lattice Boltzmann computer simulations. Our model was motivated by the observation that the equilibrium configuration of any droplet suspended on the pillar array looks like Fig. 1, i.e., a spherical cap above the posts and a bulged cylinderlike part between the posts. Hence, any droplet that is deposited on the pillar array in, for example, a purely spherical form will relax to this equilibrium shape, given that its surface contacts the sidewalls of some of the neighboring pillars. Subsequently, the droplet will move into its equilibrium position, minimizing its free energy as approximated by our free-energy model. The time scale related to shape relaxation is determined by the capillary time, which is at least one order of magnitude smaller than the second time scale related to the gradient of the free energy with respect to p . Nevertheless, in order to minimize unwanted dynamical processes and also to have better control about the initial position of the droplet, we usually put the droplet of given overall volume $V(R_{\text{eff}})$ directly in a cylinder-plus-cap form into the pillar array. The point in time when steady state is reached is determined by checking that the liquid interface does not move anymore over a sufficiently long time.

Simulation setup. In our lattice Boltzmann simulations,

we will generally fix the LB relaxation time to $\tau=0.8$, a value where our model is expected to be numerically most stable [50]. The temperature is set to $T=0.4$, giving rise to coexisting liquid and vapor densities of $\rho_L \approx 4.1$ and $\rho_V \approx 2.9$. Note that this rather small density ratio (a well-known limitation of the present LB model) is not expected to adversely affect our results since we are only concerned with the quasistatic (thermal equilibrium) behavior of a droplet. For the interface parameter κ we will use a value of 0.002. Besides that, we have also tested other values of κ and can confirm that the obtained results remain qualitatively the same.

Our simulation box consists of at least $L_x \times L_y \times L_z = 64 \times 64 \times 64$ lattice nodes; but, especially when dealing with smaller droplets, we will increase the resolution by using up to 144^3 nodes in order to minimize lattice effects. The substrate at the top of our simulation box is flat. At the bottom, it is decorated with equidistant cuboid pillars of width b , height h , and mutual center-to-center distance $d+b$ (d being the width of the gap between two neighboring pillars). When working with the 64^3 -node system, we will typically use $b=12$, $d=12$, and h around 30 lattice units (b , d , and h are rescaled accordingly for larger system sizes). These values result in $r=3.5$ for the roughness factor and $\phi=0.25$ for the pillar density. Periodic boundary conditions are applied along the x and y directions.

The width of the diffuse interface is roughly four lattice units. Since this is much smaller than the typical droplet size, we expect that the influence of this quantity on our results can be safely neglected. Possible exceptions might be situations close to depinning events, where the droplet rapidly loses contact to a large part of solid substrate. These situations are, however, not particularly relevant for the present purposes.

A. Stability of suspended droplets

1. Metastable states

The basic prediction of our free-energy model is the existence of three different (meta)stable droplet configurations, namely, (i) the CB state, which is stable given that θ_Y is larger than a certain value depending on the geometry and the droplet size; (ii) an impaled state between CB and Wenzel states that exists given that $\theta_Y < \theta_Y^{\text{lim}}$; and (iii) the Wenzel state, which is always at least metastable. In what follows, we will not consider transitions into the Wenzel state that are initiated by the contact between the lower part of the droplet and the bottom substrate (curvature-induced impalement). These issues have been studied extensively in the literature (see [23,24,36,47]). Instead, we will focus on the intrinsic stability of the CB and the impaled state by making the pillars so tall that no contact of the liquid to the bottom substrate is possible.

Examples. In Fig. 10, we first of all exemplify the typical behavior of the droplets in our simulations. Guided by the behavior of the theoretical free-energy curves (displayed in the leftmost panels), we deposit the droplet at different initial positions and wait until the droplet has settled into its equilibrium state. Since the final state of a droplet depends cru-

cially on where it is put at the beginning, the results clearly show the indication of metastability. We also notice a nice agreement with the predictions of the theoretical free-energy curves.

The analytical model is now investigated in closer detail by scanning through the $(R_{\text{eff}}, \theta_Y)$ parameter plane systematically. In order to test the stability of the CB state, we have to deposit the droplet initially with a finite penetration depth p_{init} . On one hand, a small value of p_{init} should be favored in order to make sure that we do not cross a possible free-energy barrier (see Fig. 9). On the other hand, using a too small penetration depth can lead to an immediate dissolution of the droplet from the outer pillars because the droplet can always minimize its free energy by going over into a purely spherical shape instead of penetrating into the pillars (see Sec. III A 3). This effect is not considered in our free-energy model and necessarily leads to a certain ambiguity in interpreting the simulation results. In practice, we will set the initial penetration depth $p_{\text{init}}=4$ lattice nodes when using a system size of $64 \times 64 \times 64$. When testing with higher lattice resolutions (up to $144 \times 144 \times 144$), we rescale p_{init} accordingly.

Phase diagram. In Fig. 11, the simulation results are condensed into a phase diagram and compared to the predictions of our model. Note that we have used only integer values of the contact angle; hence, the data points represent an arithmetic mean of two corresponding measurements, i.e., if we observe a state to be unstable for a value θ and stable for $\theta+1$, we plot a data point at $\theta+1/2$ to represent the phase boundary.

One can clearly see that the overall behavior of the droplet is predicted correctly by our model. In particular, the region of CB stability (i.e., regions II and III) generally increases with the droplet size. However, the boundary between a stable and unstable CB state is found to deviate from the predictions of our model quite strongly for larger droplets. We attribute this to the simplifications of our model, in particular to the fact that droplets, which are located close to the top of the pillar array, spread laterally in order to fulfill the Young condition on the flat top of each pillar [see also Fig. 13(a)].

In order to test this explanation, we recalculate the phase boundary with a refined version of our model, where the base radius a is now allowed to increase such that $\theta \leq \theta_Y$ is guaranteed for any value of p . Effectively, this means that we now fix $\theta = \theta_Y$ and consider the dependence of a on p [instead of $\theta(p)$] to determine the free-energy minima. Indeed, as the dashed curve in Fig. 11 shows, we now obtain nice agreement with the simulation results for larger droplets.

Note that the simple criterion (3) would give for our setup a value of $\theta_Y \approx 103^\circ$ below which the CB state would be unstable, independent of the droplet size. This estimate is clearly too crude for the small droplets considered here. Besides that, it also neglects possible free-energy barriers between the CB and Wenzel states, which—as our work demonstrates—are crucial to the droplet phenomenology.

The boundary for the existence of the *intermediate minimum* of the free energy is observed to lie between $\theta_Y = 106^\circ$ and 107° , in slight deviation to $\theta_Y = 109.5^\circ$ as predicted by our analytical model. This deviation can be ex-

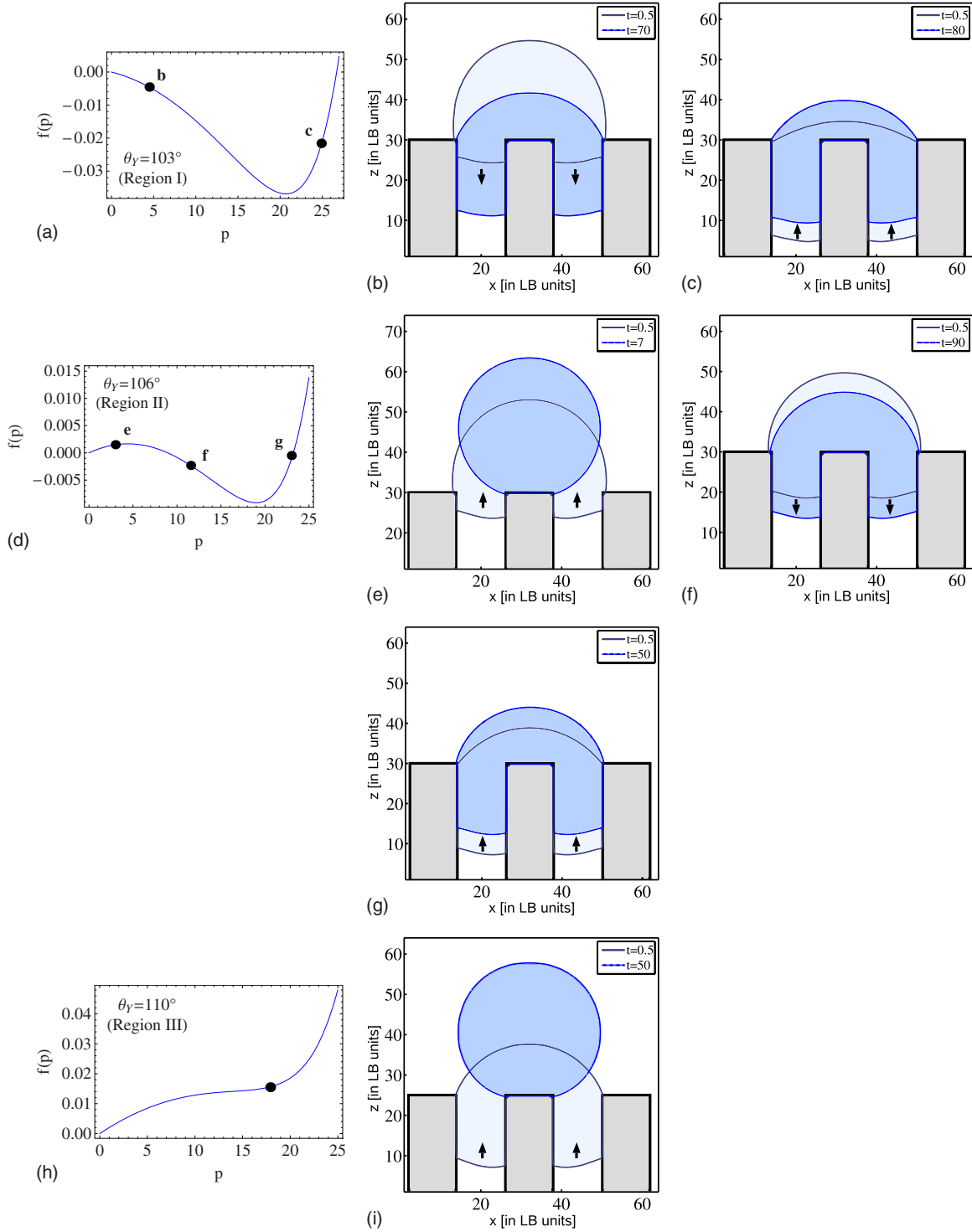


FIG. 10. (Color online) Typical droplet behavior for different contact angles and initial positions for a fixed droplet size of $R_{\text{eff}}=a$. For each case, we show in the leftmost panel the theoretical (normalized) free-energy curve and mark the initial penetration depth of the droplet with a \bullet . The arrows indicate the predicted time evolution. The simulation results, allowing us to test these predictions, are displayed in the panels on the right-hand side (simulation parameters: $b=d=12$ LB units, all times are normalized to $10^4 \approx t_c$ time steps). Regions I–III refer to the phase diagram (see Fig. 11).

plained by the fact that in reality the surface of the impaled part of the droplet is generally smaller than assumed in our model (see Fig. 3). Hence, also the contribution of the cylinder part to the total volume is smaller compared to the spherical cap part. Consequently, a smaller volume loss of

the spherical cap when the droplet impales leads to a smaller loss factor of liquid-vapor contact area. Therefore, at least for large contact angles, the overall liquid-vapor interface cannot be reduced efficiently enough to outweigh the gain in free energy due to capillary wetting.

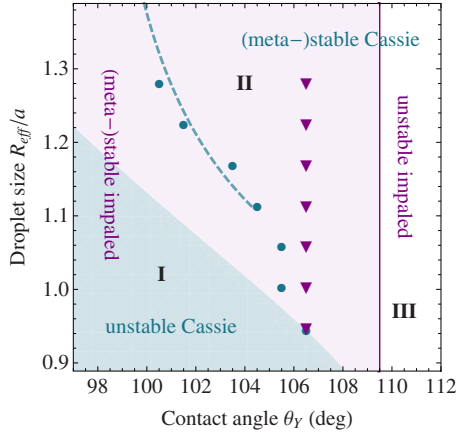


FIG. 11. (Color online) Phase diagram: stable droplet configurations in dependence of the droplet size R_{eff}/a and contact angle θ_Y (for $b=d$). Region I marks the theoretical region where the CB state is expected to be unstable. In regions II and III, the CB state is expected to be stable. The intermediate minimum of the free energy in the analytical model occurs in regions I and II. The dashed curve (---) shows the theoretical phase boundary of the CB state if the pinning condition is lifted. Symbols ($\bullet, \blacktriangledown$) depict results of our simulations: the CB state is observed to be unstable left to the filled dots (\bullet). The impaled state is found to exist left to the triangles (\blacktriangledown); that is, for larger values of the contact angle, no intermediate minimum is observed.

2. Minimum of the free energy

We now take a closer look at droplets which are residing in the intermediate minimum of the free energy. In the last section, we have already noticed that such a minimum exists below a certain θ_Y which only depends on the geometry. As another test of the predictive power of our model, we compare the penetration depths of droplets in the free-energy minimum and compare them to the theoretical expectations (Fig. 12). The penetration depth given in the plot is the average of the values measured at the three-phase contact line at the central pillar and one outer pillar.

We see that as long as the droplet is of the typical size of the array geometry (i.e., $R_{\text{eff}} \sim a$), the model is in rough agreement with the results of our simulations. In particular,

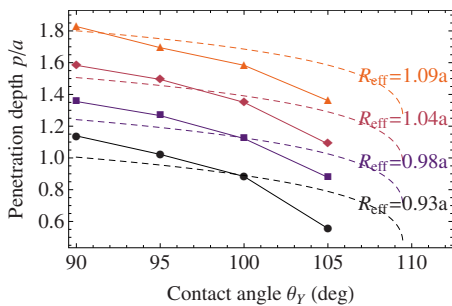


FIG. 12. (Color online) Penetration depth of a droplet at the intermediate minimum of the free energy (for the case $b=d$). For several droplet sizes R_{eff} , we compare the theoretically expected penetration depth (dashed curves) to the value obtained from LB simulations (connected symbols).

simulated curves for different droplets sizes are approximately parallel for a wide range of contact angles. A similar trend is predicted by the analytical model. The observed deviations can presumably be attributed to the fact that the contribution of the bottom part of the droplet to the total volume is overestimated by our model. A more quantitative agreement between theory and simulations is however limited by the highly nontrivial shape of the immersed part of the droplet, which is difficult to describe analytically.

3. Penetration depth in the CB state

An interesting question is now what happens to a droplet for which the model free energy predicts a vanishing (or at least very small) penetration depth? It is clear that, due to the neglect of the Gibbs condition for the apparent contact angle, the original analytical model will be increasingly inaccurate for small penetration depths and large droplet sizes. In Fig. 11 we have demonstrated that the model can in principle be adapted to take into account these constraints, however, at the price of increased complexity since the crossover region between the pinning and no-pinning regimes is hard to capture analytically.

In our simulations, we observe that for moderate values of the contact angle (i.e., $\theta_Y \lesssim 105^\circ$ for our setup) or larger values of the droplet size (i.e., $R_{\text{eff}} \gtrsim 1.1a$), a droplet deposited close to the top of the pillar array usually remains in a partly impaled CB state with a finite penetration depth [Fig. 13(a)]. The droplet spreads laterally into the grooves between the outer pillars in order to fulfill the constraint $\theta \leq \theta_Y$ on top of each pillar. This behavior is typical for large droplets and goes in line with the findings in the literature [23,24].

For larger values of the contact angle or smaller droplet sizes, we observe that the droplet usually dissolves from the sidewalls of the outer pillars and eventually attains a position just on top of the central pillar [Fig. 13(b); see also Fig. 10]. Similar behavior has also been found for nanoscale droplets [19]. The effect of detaching can be understood as a result of the competition between minimization of the liquid surface (favors a spherical form) and the free-energy cost for the creation of two interfaces (liquid-vapor and solid-vapor) from one (liquid-solid). The liquid-solid contact area generally increases with droplet size; hence, more energy is needed for dissolution. Furthermore, comparing the liquid-vapor free energy F_{LV} of a droplet within our model to a droplet in a spherical cap shape (of the same volume) sitting on top of just one pillar, we see that the relative gain in pure surface free energy $F_{\text{LV}}/F_{\text{LV,spherical cap}}$ is larger for smaller droplets [Fig. 13(c)]. Therefore, the resulting dissolution force due to surface energy minimization increases with decreasing droplet size, eventually leading to a detachment of the droplet from the sidewalls of the outer pillars.

B. Droplet evaporation

The case of a droplet evaporating from the CB state on a pillar array has been extensively studied in the literature [23–26,36,48,51]. The common observation is that evaporation can induce a transition to the Wenzel state. The mechanism for this effect is easy to understand: as the droplet de-

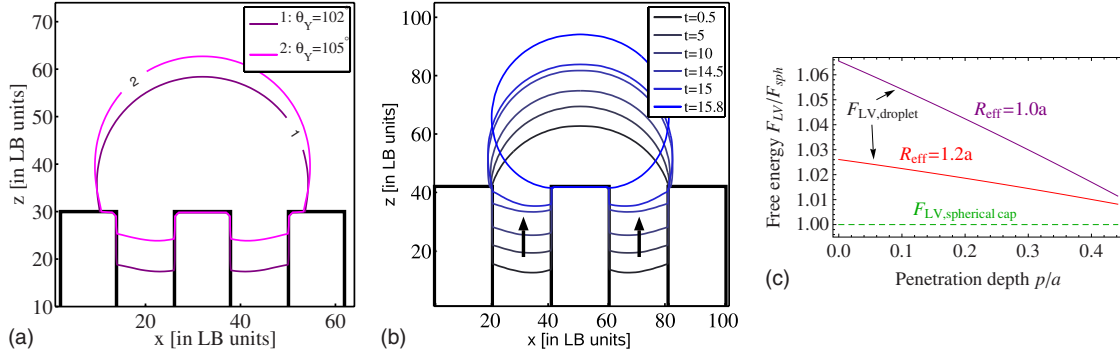


FIG. 13. (Color online) Penetration depth in the CB state. (a) Droplets in the CB state with finite penetration depth, for different contact angles θ_Y ($R_{eff}=1.2a$). (b) No residual penetration depth (detaching droplet): initially, the droplet is prepared in an impaled state and then slowly moves toward the top of the pillar array ($\theta_Y=110^\circ$, $R_{eff}=a$). Times are normalized to $10^4 \approx t_c$ LB time steps. (c) Total free energies ($F_{LV,droplet}$) of two model droplets with different sizes normalized to the free energy of corresponding droplets of a purely spherical cap form sitting on top of a single pillar ($F_{LV,spherical\ cap}$).

creases in size, the curvature of the droplet surface grows and consequently the lower part of the surface bulges more strongly. Therefore, if the pillar distance is large and the pillars are not too high, the droplet eventually touches the bottom substrate, thus initiating the transition toward the more stable Wenzel state. Furthermore, even without any nucleation of contact between the droplet and the bottom substrate, the CB state can become intrinsically unstable below a critical droplet size.

There is currently no definite conclusion in the literature about what happens to an evaporating droplet that is suspended on pillars which are so tall that no contact between liquid and bottom substrate is possible [23,26,52]. Here, we show that, as is predicted by the analytical model (see Fig. 6), if the CB state becomes unstable, the droplet is subject to a reentrant transition [34]. Consequently, it always attains a CB state at the end of the evaporation process.

In our simulation, a quasistatic evaporation is accomplished by constantly removing vapor from the volume at one horizontal plane close to the top of the simulation box (across a surface of area L^2). Some of the liquid of the droplet will then evaporate to maintain the equilibrium vapor pressure. In order to ensure that the system stays in equilibrium throughout the process, we have to estimate the correct rate for removing mass from the system. A possible candidate for the relevant time scale here is the capillary time $t_c = R/u_c$, with R as the typical length scale, in our case the radius of the droplet. The mass flux, i.e., evaporation rate per lattice node, can be approximated by

$$j \approx \frac{V_{drop}(\rho_L - \rho_G)}{t_c L^2}, \quad (16)$$

with $V_{drop} = \frac{4}{3}\pi R^3$; $\rho_L=4.1$ and $\rho_G=2.9$ as the densities (in LB units) of liquid and vapor, respectively; and L as the extent of the plane where the mass will be removed. For $L \approx 60$ and a droplet of radius $R \approx 10$ we find $j \approx 10^{-4}$. In our simulations, however, we have observed that this value of j can sometimes be too large and consequently lead to strong nonequilibrium effects that even mask the interesting phenomenon of the reentrant transition. The reason is that the motion of the

droplet along the pillar sidewall is determined by the gradient of the actual surface free energy of the droplet, $df(p)/dp$. Hence, without the knowledge of the exact free energy, one can estimate the correct evaporation rate in order to ensure quasistatic equilibrium of the droplet only after the simulation has finished. Based on that experience, we will typically take $j \approx 10^{-7}, \dots, 10^{-5}$ in our simulations.

Evaporation with reentrant transition. In Fig. 14 we focus on the evaporation process of a droplet of size $R_{eff}=1.2a$ that is initially in a stable CB state with a contact angle of $\theta_Y=103^\circ$. The stability of this state has been checked before-

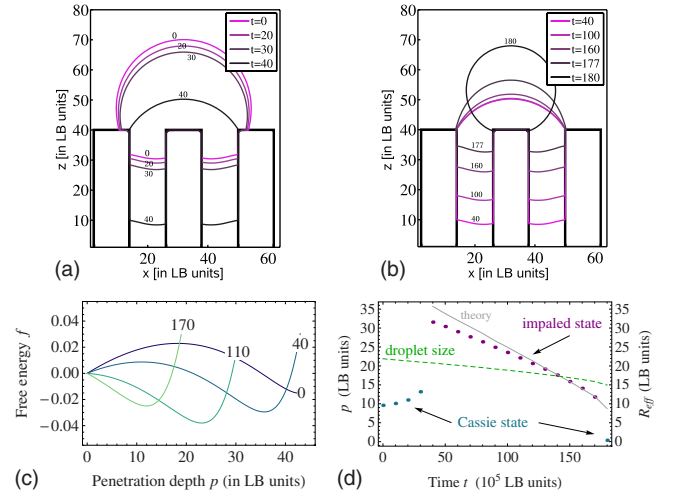


FIG. 14. (Color online) Quasistatic evaporation of a droplet ($R_{eff}=1.2a$) that is initially in a stable CB state with a Young contact angle of $\theta_Y=103^\circ$. (a) and (b) show cross sections of the evaporating droplet for successive simulation times (normalized to $10^5 \approx 10t_c$ time steps). For better visibility, the process is separated into (a) the sinking and (b) the rise of the droplet. In (c) the theoretical free-energy curves $f/4\pi\sigma_{LV}a^2$ corresponding to the selected times (indicated by the labels on each curve) are plotted. (d) shows the effective size R_{eff} of the evaporating droplet (dashed curve) and the measured penetration depth (points) together with theoretical expectation of the latter (solid line). The evaporation rate is 5×10^{-7} per LB time step, applied at a xy plane close to the top of the simulation box.

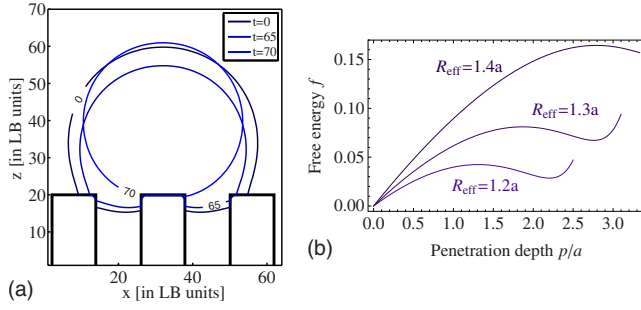


FIG. 15. (Color online) Evaporation of a small droplet ($R_{\text{eff}} = 1.4a$) that is initially in the CB state for a contact angle of $\theta_Y = 106^\circ$. In (a) cross sections at several times during the evaporation process are shown. In (b) the corresponding free-energy curves of our model are displayed. The curve for $R_{\text{eff}} = 1.2a$ belongs to the time $t = 6.5 \times 10^5$ where the droplet has just dissolved from the outer pillars. (Time t is normalized to $10^4 \approx t_c$ time steps, evaporation rate 10^{-5} .)

hand by performing a simulation without evaporation over a sufficiently long time. The stability is also suggested by the corresponding theoretical free-energy curve for $t=0$ that is plotted in Fig. 14(c). However, as explained in Sec. III, while the theoretical curve predicts a vanishing penetration depth, in our simulation the droplet resides in a partly impaled CB state at the beginning. We remark that the theoretically calculated free-energy curves are not expected to describe every detail of our simulation. Instead, they are given here to provide a basic understanding of the droplet behavior.

During evaporation, the droplet decreases in size [see Fig. 14(d)] and, while still being in the CB state, its penetration depth slightly increases. At time $t \approx 30 \times 10^5$, the CB state becomes unstable, and the droplet quickly slides down the pillars, attaining its new equilibrium position at the local minimum of the free energy.

Due to the slowness of the vapor removal, a quasistatic equilibrium is maintained throughout the process and the droplet adapts its penetration depth in accordance with the prediction of the analytical equilibrium model [given by the solid curve in Fig. 14(d)]. As expected, since the position of this minimum shifts toward smaller penetration depths as the droplet size decreases, we now find the droplet reaching back again to the top of the pillars. At $t \approx 1.77 \times 10^7$ the droplet, having lost about three quarters of its initial volume, finally re-enters the CB state again by dissolving from the pillar sidewalls and attaining a position on top of the central pillar.

Evaporation without reentrant transition. For the purpose of efficient self-cleaning surfaces it is desirable to avoid the impalement of the droplet during evaporation at all. From our previous analysis we guess that this can be achieved by several means: either one can opt for a larger gap width between the pillars, thereby reducing the maximal penetration depth, or one can choose a larger contact angle. The evaporation process using the second option is shown in Fig. 15.

Although the free-energy curves predict that the penetration depth should go toward zero, the droplet remains pinned at the outer pillars because the cost of the creation of two interfaces (liquid-vapor and solid-vapor) from one (liquid-

solid) cannot yet be provided by the capillary force (see Sec. III A 3). But, due to the evaporation, the liquid-solid contact area decreases and the lower contact line moves upward, until at time $t \approx 6.5 \times 10^5$ the droplet finally detaches from the outer pillars. This effect of detaching goes in line with the observation of contact line depinning during the evaporation of a large drop in [24].

Interestingly, previous 2D simulations of the evaporation process for similarly small droplets [24] did not observe a reentrant transition. There, the droplet was found to always immerse fully into the pillar structure. A similar behavior is observed in our simulations when a significantly larger evaporation rate is used. We therefore suspect a violated quasistatic equilibrium and the occurrence of inertial effects (i.e., acceleration of the droplet as the steepness of the free energy increases too quickly) as the probable reasons for the observations in [24]. The reentrant transition as such basically results from the pinning condition and should not be bound to a certain dimensionality.

IV. CONCLUSION

In this work, we investigated the behavior of liquid droplets on hydrophobic patterned substrates in the case where the droplets are of comparable size to the roughness scale. For this purpose, we employed numerical computer simulations based on the free-energy lattice Boltzmann method and proposed a simple three-dimensional analytical free-energy model. The results of both approaches were shown to be in good accordance.

We established the existence of a new equilibrium state of a droplet, in which the liquid is immersed in the texture, but not yet contacts the bottom surface. This impaled state is shown to originate from a generic minimum of the free energy that is expected to occur in any situation of capillary wetting by a spherical liquid reservoir. Consequently, the droplet sinks down to a finite depth, where the force of the Laplace pressure in the spherical cap (pushing the liquid into the grooves) is compensated by the repulsive force in the hydrophobic capillary.

The penetration depth of a droplet in the impaled state decreases with its size in such a way that very small droplets are always located close to the top of the surface texture. It is understood that this behavior applies only if the pillars are made so tall that no Wenzel transition can occur while the droplet penetrates. Droplets in the impaled state are expected to have Wenzel-like properties, i.e., strong pinning and a comparatively small apparent contact angle.

We further have directly demonstrated the metastability of the different wetting states, where—depending on the geometry, the microscopic contact angle, and its initial position—the droplet can end up in the CB state, the impaled state, or the Wenzel state. Using a simple analytical free-energy model, the phase boundaries for the CB and the impaled state were computed for small droplets. The observed penetration depth of droplets in the impaled state is found to be in good agreement with the theoretical predictions.

Generally, the CB state either appears with the droplet having a small residual penetration or, more specifically for

small droplets, with the droplet dissolving from most of the pillars and attaining a purely spherical shape on top of a single pillar. For large values of the contact angle, we find that the droplet always adopts a CB state even if it is deposited deeply in the pillar array (but not yet contacting the bottom substrate).

Finally, we have applied our results to the case of a droplet evaporating from a CB state—a process that is especially relevant for the efficiency of self-cleaning surfaces. Depending on the contact angle, we find that in the course of evaporation, the droplet either reaches a critical size and impales in the texture or it remains in the CB state. If the droplet becomes unstable, it first sinks down to the local minimum of the free energy, but then rises again toward the top of the pillars.

ACKNOWLEDGMENTS

We thank David Quéré for helpful discussions and Alexandre Dupuis for providing us a version of his LB code. M.G. gratefully acknowledges financial support by the Deutsche Forschungsgemeinschaft (DFG) under the Grant No. Va205/3-2 (within the Priority Program Nano & Microfluidics SPP1164). ICAMS gratefully acknowledges funding from ThyssenKrupp AG, Bayer MaterialScience AG, Salzgitter Mannesmann Forschung GmbH, Robert Bosch GmbH, Benteler Stahl/Rohr GmbH, Bayer Technology Services GmbH, and the state of North-Rhine Westphalia as well as the European Commission in the framework of the European Regional Development Fund (ERDF).

-
- [1] T. Onda, S. Shibuichi, N. Satoh, and K. Tsujii, *Langmuir* **12**, 2125 (1996).
 - [2] C. Neinhuis and W. Barthlott, *Ann. Bot. (London)* **79**, 667 (1997).
 - [3] D. Öner and T. McCarthy, *Langmuir* **16**, 7777 (2000).
 - [4] D. Quéré, *Annu. Rev. Mater. Res.* **38**, 71 (2008).
 - [5] C. Dorrier and J. Rühe, *Soft Matter* **5**, 51 (2009).
 - [6] Note that with “equilibrium” we refer to mechanical equilibrium, which requires a local minimum of the free energy and hence in general corresponds to a metastable state. In contrast, thermodynamic equilibrium is usually understood as referring to the global minimum of free energy.
 - [7] A. B. D. Cassie and S. Baxter, *Trans. Faraday Soc.* **40**, 546 (1944).
 - [8] R. N. Wenzel, *Ind. Eng. Chem.* **28**, 988 (1936).
 - [9] J. Bico, U. Thiele, and D. Quéré, *Colloids Surf., A* **206**, 41 (2002).
 - [10] R. E. Johnson and R. H. Dettre, *Contact Angle, Wettability and Adhesion* (American Chemical Society, Washington, D.C., 1964), Vol. 43, pp. 112–135.
 - [11] J. Bico, C. Marzolin, and D. Quéré, *EPL* **47**, 743 (1999).
 - [12] Z. Yoshimitsu, A. Nakajima, T. Watanabe, and K. Hashimoto, *Langmuir* **18**, 5818 (2002).
 - [13] G. Carbone and L. Mangialardi, *Eur. Phys. J. E* **16**, 67 (2005).
 - [14] A. Lafuma and D. Quéré, *Nature Mater.* **2**, 457 (2003).
 - [15] B. He, N. A. Patankar, and J. Lee, *Langmuir* **19**, 4999 (2003).
 - [16] A. Marmur, *Langmuir* **20**, 3517 (2004).
 - [17] N. A. Patankar, *Langmuir* **20**, 7097 (2004).
 - [18] C. Ishino, K. Okumura, and D. Quéré, *EPL* **68**, 419 (2004).
 - [19] T. Koishi *et al.*, *Proc. Natl. Acad. Sci. U.S.A.* **106**, 8435 (2009).
 - [20] D. Bartolo, F. Bouamrine, E. Verneuil, A. Buguin, P. Silberzan, and S. Moulinet, *EPL* **74**, 299 (2006).
 - [21] M. Reyssat, A. Pépin, F. Marty, Y. Chen, and D. Quéré, *EPL* **74**, 306 (2006).
 - [22] J. Hyväluoma and J. Timonen, *EPL* **83**, 64002 (2008).
 - [23] S. Moulinet and D. Bartolo, *Eur. Phys. J. E* **24**, 251 (2007).
 - [24] H. Kusumaatmaja, M. L. Blow, A. Dupuis, and J. M. Yeomans, *EPL* **81**, 36003 (2008).
 - [25] G. McHale, S. Aqil, N. Shirtcliffe, M. I. Newton, and H. Y. Erbil, *Langmuir* **21**, 11053 (2005).
 - [26] M. Reyssat, J. M. Yeomans, and D. Quéré, *EPL* **81**, 26006 (2008).
 - [27] C. Cottin-Bizonne, C. Barentin, E. Charlaix, L. Bocquet, and J. L. Barrat, *Eur. Phys. J. E* **15**, 427 (2004).
 - [28] P. S. Swain and R. Lipowsky, *Langmuir* **14**, 6772 (1998).
 - [29] G. Wolansky and A. Marmur, *Colloids Surf., A* **156**, 381 (1999).
 - [30] J. Jopp, H. Gröll, and R. Yerushalmi-Rozen, *Langmuir* **20**, 10015 (2004).
 - [31] D. Quéré, *Rep. Prog. Phys.* **68**, 2495 (2005).
 - [32] K. K. S. Lau *et al.*, *Nano Lett.* **3**, 1701 (2003).
 - [33] R. D. Narhe and D. A. Beysens, *Langmuir* **23**, 6486 (2007).
 - [34] M. Gross, F. Varnik, and D. Raabe, *EPL* **88**, 26002 (2009).
 - [35] A. J. Briant, A. J. Wagner, and J. M. Yeomans, *Phys. Rev. E* **69**, 031602 (2004).
 - [36] A. Dupuis and J. M. Yeomans, *Langmuir* **21**, 2624 (2005).
 - [37] F. Varnik *et al.*, *Phys. Fluids* **20**, 072104 (2008).
 - [38] N. Moradi, F. Varnik, and I. Steinbach (unpublished).
 - [39] R. Blossey, *Nature Mater.* **2**, 301 (2003).
 - [40] M. R. Swift, W. R. Osborn, and J. M. Yeomans, *Phys. Rev. Lett.* **75**, 830 (1995).
 - [41] P. G. de Gennes, *Rev. Mod. Phys.* **57**, 827 (1985).
 - [42] J. W. Cahn, *J. Chem. Phys.* **66**, 3667 (1977).
 - [43] D. Raabe, *Modell. Simul. Mater. Sci. Eng.* **12**, R13 (2004).
 - [44] S. Succi and J. M. Yeomans, *Phys. Today* **55**(12), 58 (2002).
 - [45] J. W. Gibbs, *Scientific Papers 1906* (Dover, New York, 1961), Dover reprint.
 - [46] M. Sbragaglia, A. M. Peters, C. Pirat, B. M. Borkent, R. G. H. Lammertink, M. Wessling, and D. Lohse, *Phys. Rev. Lett.* **99**, 156001 (2007).
 - [47] M. Nosonovsky and B. Bhushan, *Nano Lett.* **7**, 2633 (2007).
 - [48] Y. C. Jung and B. Bhushan, *Scr. Mater.* **57**, 1057 (2007).
 - [49] This is a consequence of the assumption that the droplet remains pinned to the edges of the pillars.
 - [50] M. R. Swift, E. Orlandini, W. R. Osborn, and J. M. Yeomans, *Phys. Rev. E* **54**, 5041 (1996).
 - [51] H. Y. Erbil, G. McHale, and M. I. Newton, *Langmuir* **18**, 2636 (2002).
 - [52] Y. C. Jung and B. Bhushan, *J. Microsc.* **229**, 127 (2008).